Wetting of polymer surfaces with hierarchical structures

Atomic layer deposition of p-type anatase $TiO_2$

Polymer-free graphene transfer method

# Stripe-like Clay Nanotubes Patterns in Glass Capillary Tubes for Capture of Tumor Cells

Mingxian Liu,* Rui He, Jing Yang, Wei Zhao, and Changren Zhou*

Department of Materials Science and Engineering, Jinan University, Guangzhou 510632, People's Republic of China

ⓢ Supporting Information

**ABSTRACT:** Here, we used capillary tubes to evaporate an aqueous dispersion of halloysite nanotubes (HNTs) in a controlled manner to prepare a patterned surface with ordered alignment of the nanotubes . Sodium polystyrenesulfonate (PSS) was added to improve the surface charges of the tubes. An increased negative charge of HNTs is realized by PSS coating (from −26.1 mV to −52.2 mV). When the HNTs aqueous dispersion concentration is higher than 10%, liquid crystal phenomenon of the dispersion is found. A typical shear flow behavior and decreased viscosity upon shear is found when HNTs dispersions with concentrations higher than 10%. Upon drying the HNTs aqueous dispersion in capillary tubes, a regular pattern is formed in the wall of the tube. The width and spacing of the bands increase with HNTs dispersion concentration and decrease with the drying temperature for a given initial concentration. Morphology results show that an ordered alignment of HNTs is found especially for the sample of 10%. The patterned surface can be used as a model for preparing PDMS molding with regular micro-/nanostructure. Also, the HNTs rough surfaces can provide much higher tumor cell capture efficiency compared to blank glass surfaces. The HNTs ordered surfaces provide promising application for biomedical areas such as biosensors.

**KEYWORDS:** patterned surface, assembly, alignment, halloysite nanotube, tumor cell
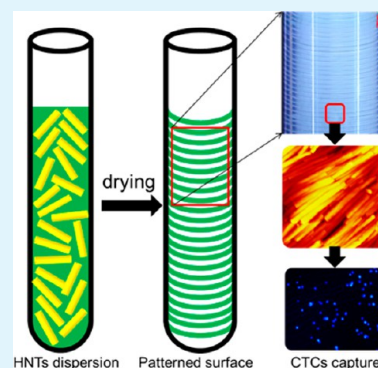
## 1. INTRODUCTION

Hierarchical assembly of nanoparticles has attracted considerable attention, as the formed ordered structures have potential applications in optics, electronics, magnetic devices, and biotechnology.[1,2] An interesting preparative strategy for hierarchical structures is to control the evaporation of nanoparticles or polymers from their solutions or dispersion.[3] This method represents a simple, nonlithographic, and top-down technique route to create ordered surface structures. The evaporative assembly into regular structures has been applied to a wide spectrum of materials, such as polymers,[4,5] viruses,[6,7] protein,[8] quantum dots,[9] latex particles,[10,11] carbon nanotubes (CNTs),[12,13] and gold nanoparticles.[14,15] The ordered structure can be formed by allowing a drop to evaporate directly[16] or in restricted environments by a confined geometry.[3,17] The confined geometry includes two parallel plates, sphere-on-flat, cylinder-on-flat, glass capillary, and curve-on-flat, etc. For different confined geometry, the formed pattern structures are largely different. The typical samples are a gradient concentric ring, gradient stripes, or bands. The evaporative flux, solution concentration, and interfacial interaction between the solvent, the solute, and the substrate, etc., have significant effect on the surface structure formation. On the other hand, preferential alignment of anisotropic nanoparticles such as nanotubes,[18] nanofibers,[19] nanorods,[15] and nanowires[20] can enhance their electrical, electrochemical, optical, and electromechanical properties along the orientation line. However, little results of the evaporative assembly were yet reported on one-dimensional

nanoclays which are promising natural materials for many applications.

Halloysite nanotubes (HNTs, $Al_2Si_2O_5(OH)_4 \cdot nH_2O$) are novel one-dimensional nanoparticles with tubular morphology which are available in abundance in many countries and recently become the subject of research attention as a new type of material.[21−24] HNTs have diameters of 20−50 nm and lengths of 200−1000 nm, which give a high aspect ratio of 10−100. HNTs possess large specific surface areas and abundant hydroxyl groups on their surfaces, and they also are environmentally friendly and biocompatible.[25] Therefore, HNTs have shown promising applications as nanoadditives for enhancing the mechanical performances, thermal stability, and nucleating agents for polymers.[21,26,27] Due to their unique tubular structure and good nanosafety, recent studies show that they are good candidates as cell growth supporting scaffolds, a drug-controlled delivery platform, and biosensors and for enzyme immobilization.[22,25,28−35] However, few reports have focused the basic understating of their self-assembly behavior of HNTs under certain conditions. Luo et al. investigated the liquid crystalline phase behavior and sol−gel transition of HNTs aqueous dispersions.[36] They found that completely ordered alignments of the tubes and the liquid crystalline network of HNTs were obtained when the aqueous dispersion

concentration was higher than 25 wt %. Very recently, Zhao et al. prepared highly ordered patterns of HNTs with droplet-casting evaporation of HNTs dispersion.[16] HNTs formed into a "'coffee-ring'" deposit and aligned along the droplet edge when drying the dispersion. However, the droplet-casting technology is limited to their ability to fabricate uniformly aligned HNTs over a large area.

In this study, we used glass capillary tubes to control evaporation of HNTs aqueous dispersion to prepare a patterned surface with ordered nanotube alignment. To stabilize the HNTs dispersion, sodium poly(styrenesulfonate) (PSS) was added to improve the surface charges of the tubes.[16,37,38] Upon drying the HNTs aqueous dispersion in glass tubes, a regular pattern is formed in the wall of the tube. The width and spacing of the bands were dependent on the HNTs dispersion concentration and the drying temperature. The patterned surface can be used as a model for preparing PDMS molding with regular micro-/nanostructure. Also, the rough surfaces of HNTs can provide much higher tumor cell capture efficiency compared to blank glass surfaces. This provides new opportunities for application of HNTs in miniaturized electronics, photonics, catalysts, nanotechnology, and biotechnology.

## 2. EXPERIMENTAL SECTION

**2.1. Materials.** Hallysite nanotubes (HNTs) were purchased from Guangzhou Runwo Materials Technology Co., Ltd., China. The elemental composition of the HNTs by X-ray fluorescence (XRF) was determined as follows (wt %): $SiO_2$, 54.29; $Al_2O_3$, 44.51; $Fe_2O_3$, 0.63; $TiO_2$, 0.006. Before using, HNTs were purified according to the procedure in ref 39. The Brunauer–Emmett–Teller (BET) surface area of the used HNTs was 50.4 $m^2$/g. PSS (MW 70,000) and 3-aminopropyltriethoxysilane (APTES) were purchased from Sigma-Aldrich. All other chemicals were used as purchased (Aladdin) without further purification. Ultrapure water from a Milli-Q water system was used to prepare the aqueous dispersion.

**2.2. Functionalization of HNTs by PSS.** Functionalization of HNTs by PSS was performed according to a previous report with a slight modification.[16] A 2 g amount of PSS was dispersed in 100 mL of deionized water in a flask and stirred for 30 min to form a transparent solution. Then, 2 g of HNTs were added gradually under continuous stirring in this solution for 48 h at room temperature. Then the dispersion was collected and centrifuged at 4000 rpm for 10 min. The precipitated HNTs were washed 3 times with deionized water. Finally, the obtained solid was dried in a vacuum drier for 24 h at 50 °C and crushed into powder by mortar before use. The samples were denoted as PSS-HNTs.

**2.3. Evaporation of PSS-HNTs Aqueous Dispersion.** Evaporative self-assembly of PSS-HNTs was performed in glass tubes. About 5 mL of PSS-HNTs aqueous dispersion (2%, 5%, 10%, and 20%; mass fraction) was cast into the tubes (inner diameter × height: 7 × 100 $mm^2$). The evaporation took place at 60, 70, 80, and 90 °C under oven without blast. Approximately 5 days were needed to dry the PSS-HNTs dispersion to equilibrium state at 60 °C. The result reported here were robust and reproducible. We also tried to dry the dispersion at room temperature. The drying time was too long when drying the dispersion (several months) at room temperature. Afterward, the tube was scraped and the patterns on the internal wall of the tube were examined.

**2.4. Characterization.** *ζ-Potential Measurement.* The ζ-potentials of dilute HNTs aqueous dispersions, PSS-HNTs aqueous dispersions, and PSS solution were measured using a Zetasizer Nano ZS instrument (Malvern Ltd., U.K.). Prior to each measurement, the operating conditions were checked and adjusted using a calibrated latex dispersion supplied by the instrument manufacturer (ζ-potential, −50 ± 5 mV).

*Transmission Electron Microscopy.* The dilute PSS-HNTs aqueous dispersions were dipped and dried on the carbon-film-supported Cu grid. Then the samples were observed using Philips Tecnai 10 transmission electron microscopy (TEM) instrument under accelerating voltage of 100 kV.

*Dynamic Light Scattering.* Hydrodynamic diameter and size distribution of PSS-HNTs solution (0.05%) were detected by a Nano-ZS instrument (Malvern Instrument). The hydrodynamic diameter was analyzed by cumulants. Samples were preserved in a 4 °C refrigerator.

*Rheological Measurements.* The rheological measurements of the PSS-HNTs dispersions with different concentrations were performed on a stress-controlled rheometer (TA-AR2000EX, TA Instruments) equipped with a cone-and-plate geometry (diameter, 40 mm; angle, 1°). The frequency sweep was performed over the frequency range of 0.01−100 Hz at the fixed strain of 0.5%.

*Polarized Optical Micrographs.* Drops of PSS-HNTs dispersion were cast and sandwiched between two glass slides to form the film with a thickness of about 50 $\mu$m, and then the photographs were taken by using the ZEISS SteREO Discovery V20 (Oberkochen, Germany) polarized optical microscope.

*Stereomicroscope.* The morphology of the patterned surfaces was examined using the ZEISS SteREO Discovery V20 instrument. The photographs were taken at the different magnifications.

*Scanning Electron Microscope.* The scanning electron microscope (SEM) images of the patterned surfaces were obtained with a Zeiss Ultra 55 SEM machine at 5 kV. In order to quantify the degree of the tubes' alignments, ImageJ software was used to measure the angles of the tubes with respect to one direction.

*Atomic Force Microscopy.* Morphology of the patterned surfaces was observed with a multimode atomic force microscopy (AFM) instrument with NanoScope IIIa controller (Veeco Instruments Inc.). The experiment was performed at 25 °C.

*Contact Angle Measurement.* The contact angles were measured with a KRUSS drop-shape analyzer DSA 100 instrument at 25.0 ± 0.1 °C. The contact angle was measured just after the liquid deposition onto the substrate. The liquid droplet volume was 5.0 ± 0.5 $\mu$L. Five measurements at least were carried out on each sample. For the HNTs samples, the HNTs powder was pelleted by a universal tablet compression machine. $\theta_{SG}$ and $\theta_{SN}$ were obtained by measuring the contact angle of the different PSS-HNTs dispersions on the glass and the HNTs surfaces.

**2.5. Preparation and Characterization of PDMS Ordered Pattern by HNTs Stripes.** The ordered structure of poly(dimethylsiloxane) (PDMS) film was prepared by a casting technique. We poured PDMS precursor liquid mixed with the curing agent (10:1 by weight) on the freshly prepared HNTs pattern (template). After curing the PDMS at 70 °C for about 2 h, the template was removed. The PDMS films were then washed with ethanol under ultrasonic treatment, and stripe-like structures were obtained.

**2.6. Capture of Tumor Cells by the HNTs Pattern Surfaces.** The sterilized PSS-HNTs pattern surfaces formed by 10% PSS-HNTs dispersion (hydrophobization treatment by APTES, Supporting Information Figure S1) were placed into 24-well cell culture plates. Then, cell suspensions (2 mL, $10^4$ cells/mL) were carefully added into each well for the predetermined capture time. Afterward, the substrates were taken out of the cell suspensions and rinsed carefully five times with PBS for 2−3 times. After the cells were fixed using paraformaldehyde solution (4 wt % in PBS), penetrated using Triton-X100 (0.2 wt % in PBS), and dyed using 4′,6-diamidino-2-phenylindole (DAPI) solution (5 $\mu$g·$mL^{-1}$ in PBS), the substrates were imaged using fluorescence microscopy (OLYMPUS, IX35, Japan). The cell numbers captured on the substrate were counted using ImageJ software. Then, by comparing that number with the total number of cells added, we calculated the capture efficiency.

## 3. RESULTS AND DISCUSSION

**3.1. Functionalization of HNTs by PSS.** A good dispersion state of HNTs can be realized via ultrasonic

treatment as shown in Figure 1a, which is due to the small dimension and the electrostatic repulsion interactions of the
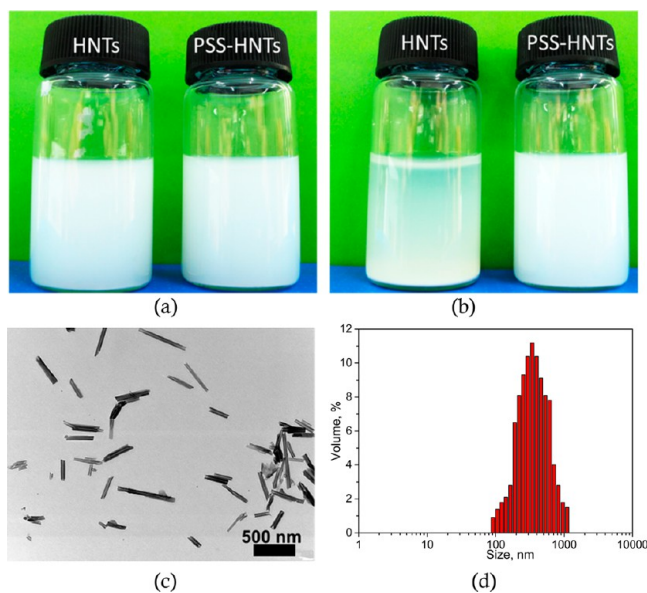


**Figure 1.** Photographs of raw HNTs and PSS-HNTs aqueous dispersions(a) and the same after 24 h (b) with concentration of 5%. TEM image (c) and size distribution by DLS (d) of PSS-HNTs.

tubes. However, sedimentation of HNTs is found after stopping the ultrosonication treatment. The low stability of the HNTs aqueous dispersion is detrimental to their evaporation-induced self-assembly. The physical adsorption of polyelectrolyte can alter the nature of the clay mineral surfaces and improve their surface physical and chemical properties.[40] The anionic PSS can selectively adsorb on the positive alumina surface of the nanotube due to electrostatic interactions, which leads to the increase in the dispersion stability of HNTs in aqueous dispersion.[16,37] From Figure 1b, no sedimentation of PSS-HNTs dispersion can be found after stopping of ultrasonication for 24 h. A diluted PSS-HNTs dispersion gives rise to the Tyndall effect, in which a laser beam passing through a colloidal solution leaves a discernible track as a result of light scattering (Figure S2). The $\zeta$-potential for HNTs, PSS, and PSS-HNTs were also measured. The negative charge of raw HNTs and PSS in water generates the $\zeta$-potential value of $-26.1$ and $-45.6$ mV, respectively. PSS-HNTs enhance the negative $\zeta$-potential of HNTs up to $-52.2$ mV. PSS can be entrapped into the HNTs lumen, which cancels out the inner positive charges. This process creates an increase in the total negative charge of HNTs, which leads to increased electrostatic repulsions among the tubes. As a result, PSS functionalized HNTs are stabilized in aqueous dispersion. These results are consistent with previous studies.[37,41]

To characterize the size distribution of PSS-HNTs in solution, PSS-HNTs were further studied by TEM and dynamic light scattering (DLS). The results are shown in Figure 1c,d. It can be seen that the nanotubes have dimensions comparable to those of pristine HNTs. This means that the adsorption of PSS does not alter the tubular morphology. Moreover, the hollow cavity of HNTs is preserved in the PSS-HNTs. The hydrodynamic diameter of the PSS-HNTs is measured as 329.5 nm with a relatively narrow size distribution (PDI =

0.237). These also suggest PSS can facilitate the dispersion of HNTs in aqueous dispersion.

The optical properties of PSS-HNTs aqueous dispersions were investigated by polarized optical micrograph (POM) technique. Generally, the optical-pass difference in light under crossed polarizers can make a liquid crystal sample show interference colors. When examined in crossed polarizers light, the dispersion shows interference colors transferring from blue to dark yellow as the dispersion concentration increases. When the HNTs concentration is 2% or lower, the dispersion is nearly isotropic and only very weak bright domains can be identified (Figure 2a). At HNTs concentration larger than 2%, the
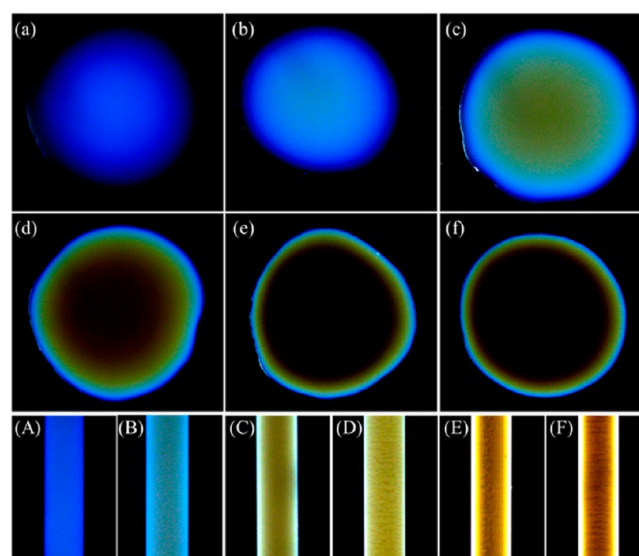


**Figure 2.** Polarized light image of a drop of PSS-HNTs dispersion with concentration of 2% (a), 5% (b), 10% (c), 20% (d), 30% (e), and 40% (f). (A–F) comparison of the different PSS-HNTs dispersions in capillary tubes under crossed polarizers (from left to right: 2–40% concentration).

gradual emergence of bright blue spots indicates the formation of ordered mesophases. With increasing HNTs dispersion concentration, the optical textures become stronger and yellow color is found in the central section of the drops. As HNTs concentration increases to 20%, the dispersion shows birefringence with intense colors, suggesting the formation of the lyotropic liquid crystalline phase. The typical birefringences are shown in Figure 2A–F. The arrangements of the nanotubes in their dispersion with different concentrations were also studied by a POM in transmission mode. In this case, a PSS-HNTs aqueous dispersion was deposited on a flat glass slide between a pair of crossed polarizers to collect its POM images (Figure 3). The emergence of birefringence domains declares the isotropic–nematic phase transition that starts at concentration of 5%. Upon increasing the concentration to 10%, the stable birefringence spreads across the whole dispersion and displays vivid Schlieren texture, which represents a typical texture of nematic phases. The large area of Schlieren textures implies uniform orientation ordering in the samples. The formed liquid crystal phase of HNTs in aqueous dispersion highly agrees with the graphene oxide (GO)[37] and montmorillonite.[42] The formation of the liquid crystals of PSS-HNTs is attributed to the high aspect ratio, the nanoscale dimension of the tube, and the high electrostatic repulsion between the tubes due to the PSS functionalization. The formation of liquid
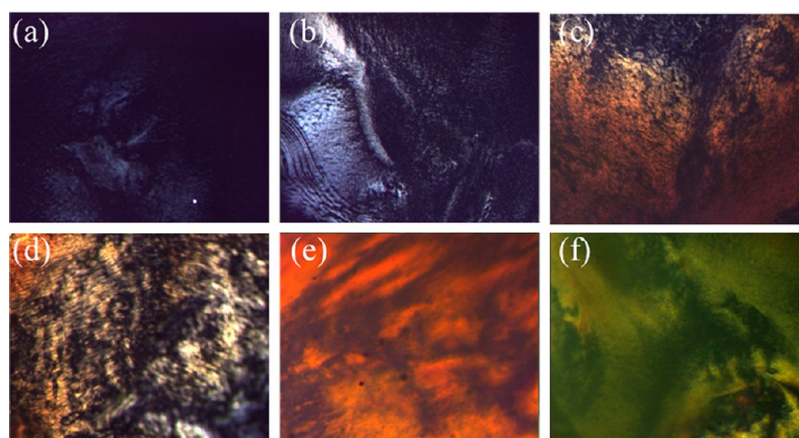
**Figure 3.** POM microscopic images of PSS-HNTs aqueous dispersions with different concentrations: (a) 2%; (b) 5%; (c) 10%; (d) 20%; (e) 30%; (f)40%.

crystal in the PSS-HNTs dispersion is critical for the subsequent assembly of the nanotubes into ordered patterns.

To further study the microstructure of PSS-HNTs dispersions with different concentrations, rheological measurement was performed. The changes of shear viscosity as functions of angular frequency of the dispersions are shown in Figure S3. The shear viscosity of all of the samples decreases when increasing the angular frequency. When comparing the different samples, the higher the concentration of the dispersion is, the higher the shear viscosity is. This is attributed to the formation of three-dimensional networks via the physical interactions especially at relatively high nanotube concentration.[36] The viscoelastic response of the dispersion system changes from the liquid-like to solid-like behaviors when the concentration is above 20%. A significant decrease of the shear viscosity (shear flow behavior) of the dispersion is observed for the samples of 20% and 40% concentration. This is because of the deformation of the existing network structure upon high shear frequency.[36]

**3.2. Evaporation of HNTs Aqueous Dispersion in a Glass Tube.** Figure 4 shows the optical images of formed HNTs patterns of drying the dispersion at 60 °C. Highly ordered stripes are formed on the inner surface of the tubes, except in the bottom region where the HNTs dispersion is hardly dried completely at the evaporation temperature. The formation of the stripes propagates from the capillary top of the liquid column toward the bottom of the tube. The formation process can be depicted as follows. Evaporative loss of water in the PSS-HNTs dispersion triggers the transportation of the HNTs to the capillary tube edge, leading to the formation of the outmost "coffee ring" (i.e., pinning of the contact line at the dispersion/air interface; "stick" step). As the level of the fluid bath drops because of the evaporation, the length of the column of the HNTs dispersion in the capillary increases relative to the surface of the dispersion in the reservoir in time until the capillary forces can no longer counterbalance the gravitational force. This causes the contact line to jump to a new position (i.e., "slip" step) and reach another equilibrium position where the dispersion is back in contact with the glass surface.[4,5,8,10] And afterward, a new ring is thus developed. Consecutive "stick–slip" cycles repeat periodically, which leads to the regular assemblies of HNTs stripes. The total process of the formation of stripes is governed by the competition between the capillary force and the pinning force. Only at the end of the
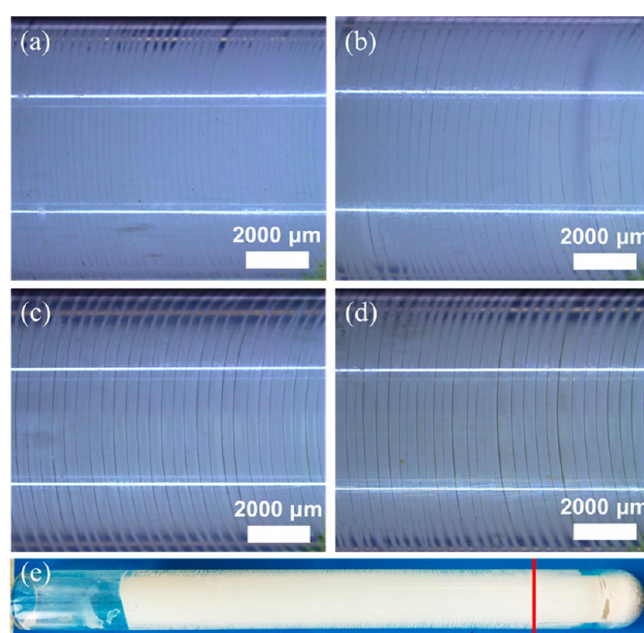


**Figure 4.** Optical images of stripe patterns formed along the capillaries for different concentrations of the PSS-HNTs aqueous dispersion dried at 60 °C: (a) 2%; (b) 5%; (c) 10%; (d) 20%. (e) Photograph of the whole glass tube with the formed HNTs stripes on the inner wall. No regular stripes are formed at the end of the glass tube below the red line.

glass tube (about one-fifth of the dispersion height), no regular stripes are formed on the inner wall of the glass tube (Figure 4e). This is due to the increased length of diffusion of the vapor to the exit of the tube at the late stage of drying, which leads to a decrease in the rate of fall of the liquid level in the reservoir. Therefore, no stripes are found in the end of the glass tube but continuous HNTs coating with some big cracks is formed in the wall. On the other hand, the HNTs dispersion concentration increases at the late stage of drying due to the slow sedimentation of the HNTs. The increased concentration of the dispersion leads to the increased density of the dispersion ($\rho$). The force balance is largely different from that of the dispersion located in the top and the middle of the tube.

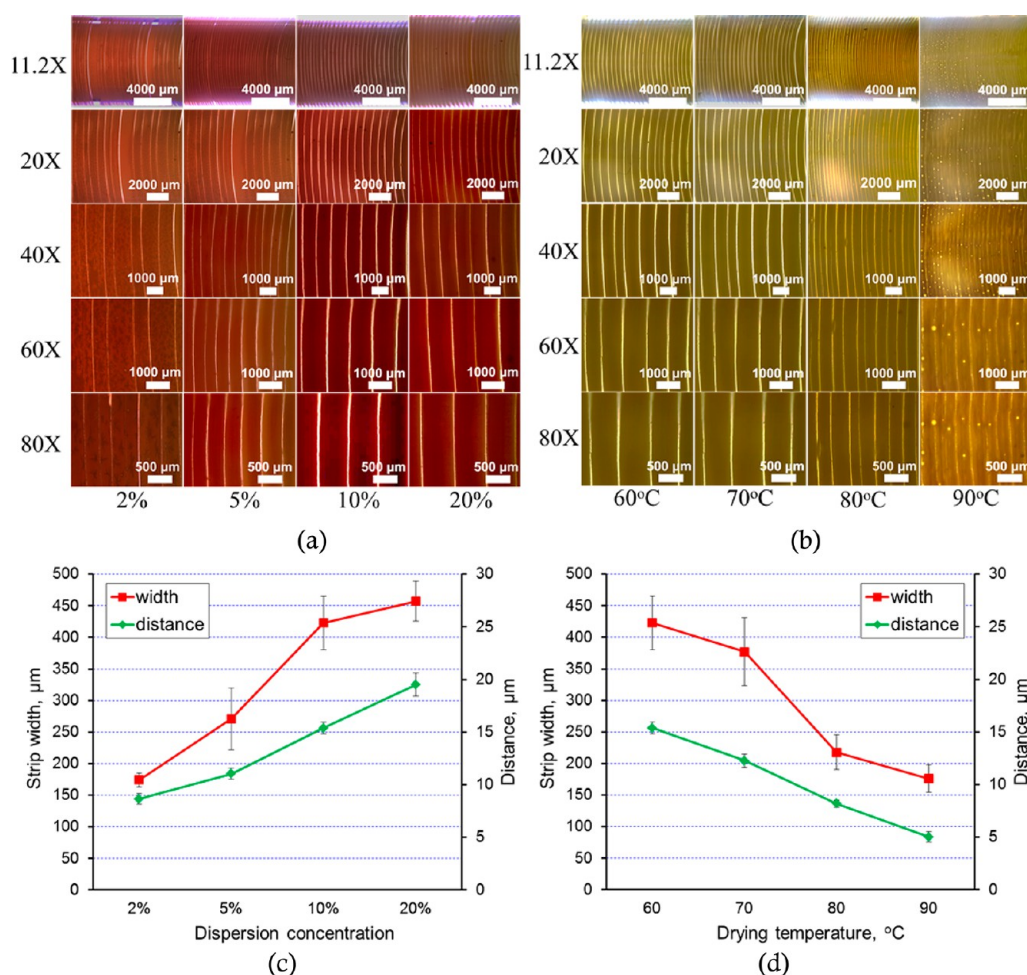In order to investigate the formed stripes structure for different HNTs concentrations, stereoscopic micrographs of

**Figure 5.** Optical microscopy images of the formed HNTs pattern surfaces in different magnifications and different concentrations: HNTs at different (a) concentrations and (b) drying temperatures. The relationship of the stripe width, the distance between the adjacent stripes, and the HNTs concentration (c) and the dry temperature (d).

these patterned surfaces were taken. Figure 5a shows the optical images of the formed stripes with different magnification. Locally, the stripes appear as parallel. In the edge of the tube, it can be seen the stripes have a certain radian. The stripe width (W) and the distance between the adjacent stripes (λ) is in the range of 175−450 μm and 10−20 μm. Figure 5c shows the variation of the W and λ with the dispersion concentration. It is clear that both W and λ increase with the concentration of the dispersion. The formation of ordered stripes is a direct consequence of the competition between the nonlinear capillary force and the linear pinning force (gravity). As concentrations of HNTs dispersions increase, the densities of the dispersions increase and the force balance is different from the samples. The dispersions with high HNTs concentration can slip to the longer distance. Therefore, the W and λ are larger for the sample of high HNTs concentration. Previous study also showed that the width and the spacing of the stripes increase with the dispersion concentration.[11] The width of the HNTs stripes is much larger than that of quantum dot rings produced by evaporation-induced self-assembly in sphere-on-flat geometry.[36] This is due to the difference in the nanoparticle, solvent, and the solution concentration.

We further investigate the influence of the drying temperature on the formation of the stripes. From Figure 5b, ordered stripes produced by evaporation of 10% HNTs can be formed

at all of the experiment temperatures (60−90 °C). At high drying temperature, some white points can be found on the ordered stripes, which may be attributed to the defects induced by the high evaporation rate of the vapor. The relationship of the W and λ with drying temperature is plotted in Figure 5d. The stripes produced at drying temperature of 60 °C have a maximum W and λ value. W and λ value linearly decrease with the increase in the drying temperature. For example, the W and λ are 175 and 5 μm upon drying the 10% HNTs dispersion, respectively. This is attributed to the high evaporation temperature promoteing the stick−slip movement of the nanotube dispersions.

The formation of regular stripes can be understood as a direct consequence of controlled, repetitive stick−slip motion of the contact line that resulted from the competition between pinning force and capillary force (depinning force) during the course of irreversible solvent evaporation.[11,43] A model for these stripes formation, which incorporates evaporation and surface properties, may be constructed by noting that the solvent is first in contact with the glass capillary. An equation of the W is given as Δh. Figure 6 shows the formed stripes on the glass capillary inner wall and the parameters for the calculation. Table 1 shows the calculation result of the W by the equation and comparison between the experimental values. It can be seen that the W matches well with nearly all parts of the glass
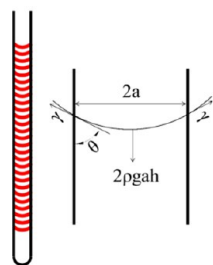
**Figure 6.** Schematics of the formed stripes on the glass capillary inner wall and the parameters for the calculation.

tube (except the end of the tube) based on the equation. This is because of the constant radius of curvature of the meniscus of the PSS-HNTs dispersion throughout the evaporation process.

$$\int_{h+\Delta h}^{h} 2\rho gah \, dh = 2 \int_{F_{SN}}^{F_{SG}} dF + F_c$$

$$F_{SG} = \gamma \cos \theta_{SG} \qquad F_{SN} = \gamma \cos \theta_{SN}$$

$$\Delta h = \frac{\gamma(\cos \theta_{SG} - \cos \theta_{SN}) + F_c}{\rho ga}$$

Here, $\Delta h$ is the width of the stripes; $\rho$ is the density of the dispersion liquid; $\gamma$ is the surface tension of the dispersion liquid; $\theta_{SG}$ is the contact angle of the dispersion liquid and the surface of the glass; $\theta_{SN}$ is the contact angle of the dispersion liquid and the nanosurface of the stripes; $g$ is the gravitational acceleration, 9.788 N/kg; $a$ is the radius of the glass tube; $F_c$ is the corrected factor, which is related to the buoyancy of the liquid, attraction of nanoparticles and dried band, force of friction, and so on. When the concentration of the dispersion liquid is low, $F_c$ is almost zero.

To illustrate the microstructure of the formed stripes, SEM was performed on the samples. Figure 7 shows the SEM microstructure and histograms of HNTs angular distribution. Consistent with the optical microcopy result, ordered stripes are observed for all of the samples. The $W$ and $\lambda$ values increase with the dispersion concentration. By examining the stripes at high magnification, one can see the formation of regular patterns of the stripes. For the 2% PSS-HNTs dispersion, the arrangement of the HNTs is disorder in the stripes (half-height peak width (HPW), 166.34°) and no pattern can be identified. Axial disclinations are observed for the samples of 5% PSS-HNTs dispersion and the HPW of the HNTs angular distribution is 81.63°. A high degree alignment of the HNTs is found in the stripes for the sample of 10% concentration (HPW, 10.44°). With high HNTs concentration (20%), the stripes have a decreased alignment degree (HPW, 65.45°). It is concluded that the change of the alignment of the HNTs in the stripes is related to the concentration of the PSS-HNTs dispersion. The HNTs concentration has a significant effect on the alignment of the HNTs. When the HNTs dispersion

concentration increases to a critical value, the nanotubes may transition to a liquid crystalline phase (as shown in the POM result) and will align parallel to the edge. The parallel orientation is mainly due to the development of a flow-induced torque on the nanotubes as one of their ends becomes pinned by the contact line and, therefore, their axial flow directions change to parallel to the edge because of the geometrical constraints.[16] In the present system, the 10% HNTs concentration may be the critical value for the high alignment of nanotubes.

Figure 8 shows the AFM images of the formed HNTs patterns. The length and diameter of HNTs have no significant difference among the samples. Consistent with previous SEM results, drying the 2% PSS-HNTs dispersion leads to an unordered alignment pattern. Drying the 5% PSS-HNTs sample in the glass capillary tubes can form disclination patterns. The stripes produced by drying the 10% PSS-HNTs have a highly ordered pattern structure. A slight decreased alignment of the tubes is found at the stripes produced by drying the 20% PSS-HNTs' dispersions. Therefore, from the SEM and AFM results, the formation of the ordered HNTs patterns is influenced by the dispersion concentration. Compared with the ordered HNTs patterns prepared via drying a drop of an aqueous HNTs suspension,[16] the present routine is a method of obtaining aligned HNTs over a large area.

The crack between the adjacent stripes was further investigated by SEM and 3D morphology analysis. Clearly, the dark notches seen in Figure 9 are microscopic channels (i.e., cracks) with approximately 10−20 $\mu$m width as revealed by SEM, which is consistent with previous optical image results. The crack is separated by the HNTs arrays patterns of a width in the range of 150−450 $\mu$m. No HNTs are in the cracks. The edges of the cracks are very sharp; the thickness of the HNTs pattern was quantified by the 3D morphology analysis (Figure 9c,d). It can be seen that the HNTs pattern is composed of several layers of nanotubes (Figure 9b,d) with thickness (depth of the crack) of ~125 $\mu$m. The three-dimensional surface roughness curve of the pattern structure formed by the 10% PSS-HNTs dispersion dried at 60 °C also shows the regular crack distribution (Figure S4).The formation of cracks arises from the competition between the stress relaxation due to the crack opening that fractured the film and the stress increase from the evaporative loss of water.[44,45]

The prepared regular HNTs cracks can be used as templates to produce ordered stripes. Liquid PDMS was cast on the HNTs patterned surface sample. The PDMS stripes were obtained by cross-linking the PDMS at room temperature for 30 min and followed by ultrasonication in ethanol for 30 min. Figure 10 shows the SEM of the stripes prepared by different HNTs patterns. It can be seen the regular PDMS stripes are successfully obtained by employing the microchannel template of HNTs produced via constrained evaporation of PSS-HNTs dispersion. The shape and size of PDMS stripes reflect the

**Table 1. Calculation of the Widths of the Stripes and Comparison with Experimental Values**

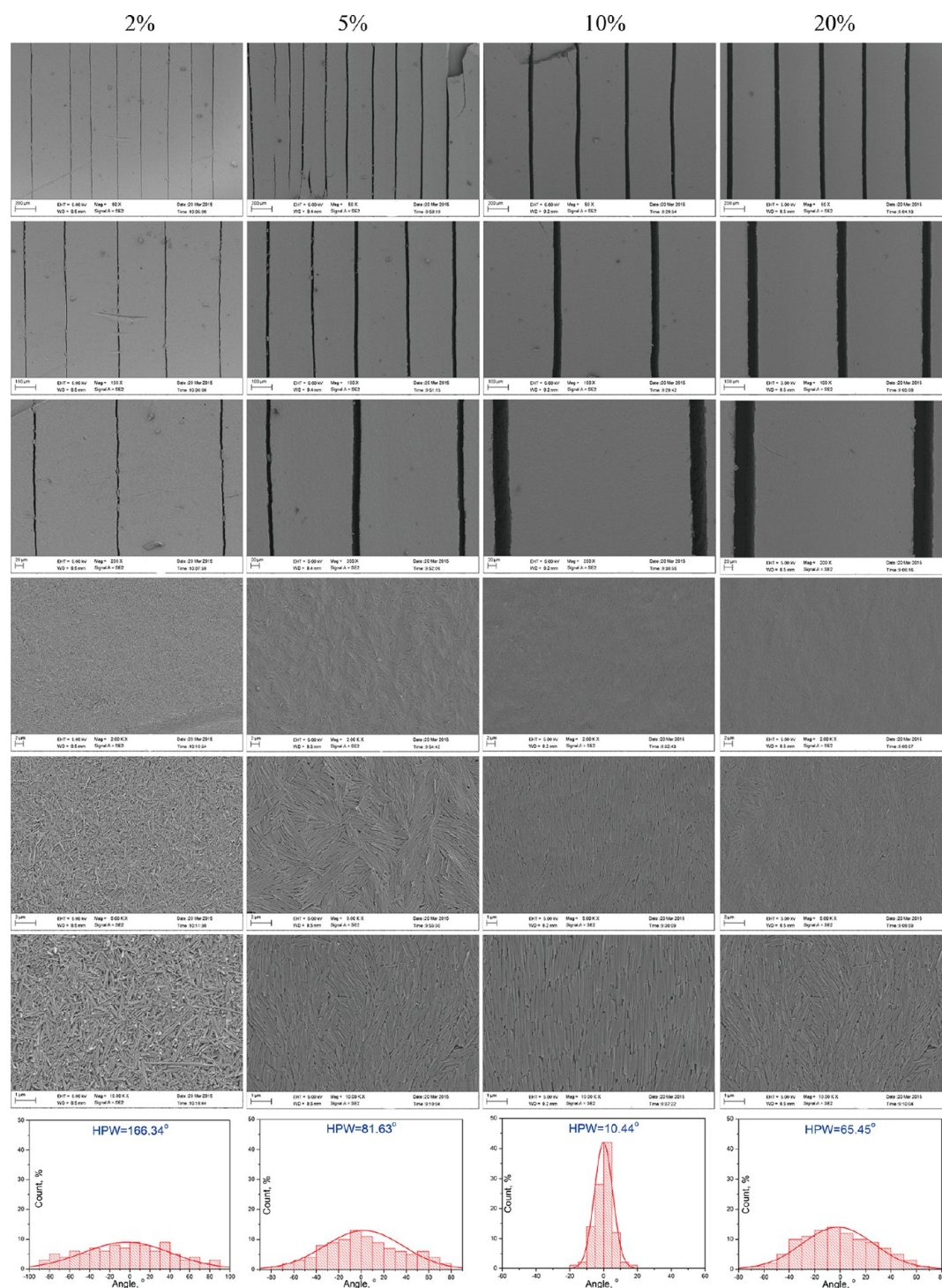| concn (wt %) | $\rho$ (kg/m$^3$) | $\gamma$ (mN/m) | $a$ (m) | $G$ (N/kg) | $\theta_{SG}$ (deg) | $\cos \theta_{SG}$ | $\theta_{SN}$ (deg) | $\cos \theta_{SN}$ | $\Delta h$ ($\mu$m) | measd value ($\mu$m) |
|---|---|---|---|---|---|---|---|---|---|---|
| 2 | 1003 | 72.24 | 0.004 | 9.788 | 29.1 | 0.874 | 38.3 | 0.785 | 163.72 | 174.32 |
| 5 | 1025 | 74.51 | 0.004 | 9.788 | 31.7 | 0.851 | 44.1 | 0.718 | 246.35 | 270.86 |
| 10 | 1053 | 75.34 | 0.004 | 9.788 | 32.6 | 0.842 | 49.6 | 0.648 | 355.13 | 422.89 |
| 20 | 1148 | 76.76 | 0.004 | 9.788 | 33.9 | 0.830 | 51.4 | 0.624 | 352.04 | 457.11 |

**Figure 7.** SEM images of the formed HNTs patterns with different concentrations and histograms of HNTs angular distribution at corresponding dispersion concentration. The curve in each histogram is fitted by Gaussian equation based on the histogram data. The angle distribution histograms were obtained by statistical analysis of angular distribution of ~200 HNTs particles.

arrangement of microchannels and are not nearly affected by the ultrasonication treatment. The stripes formed on the 2% HNTs pattern are thin, and the height is low. The 10% HNTs surface gives excellent regular stripes of PDMS. The width and height of the PDMS stripes are approximately 15 and 120 $\mu$m, respectively. This is in agreement with the previous optical microscopy image and SEM result. Previous study also found that the regular polystyrene nanoparticle microchannels could

be exploited as templates to produce well-ordered gold stripes.[45]

**3.3. Capture of Tumor Cells by the HNTs Pattern Surfaces.** Recent research showed that nanometer-scale topography influences diverse cell behaviors, including cell adhesion, cell orientation, and cell motility.[46,47] The nanometer-scale topography can enhance interactions between the substrate and different target cells such as T lymphocytes and tumor cells.[38,48,49] These findings inspired us to achieve
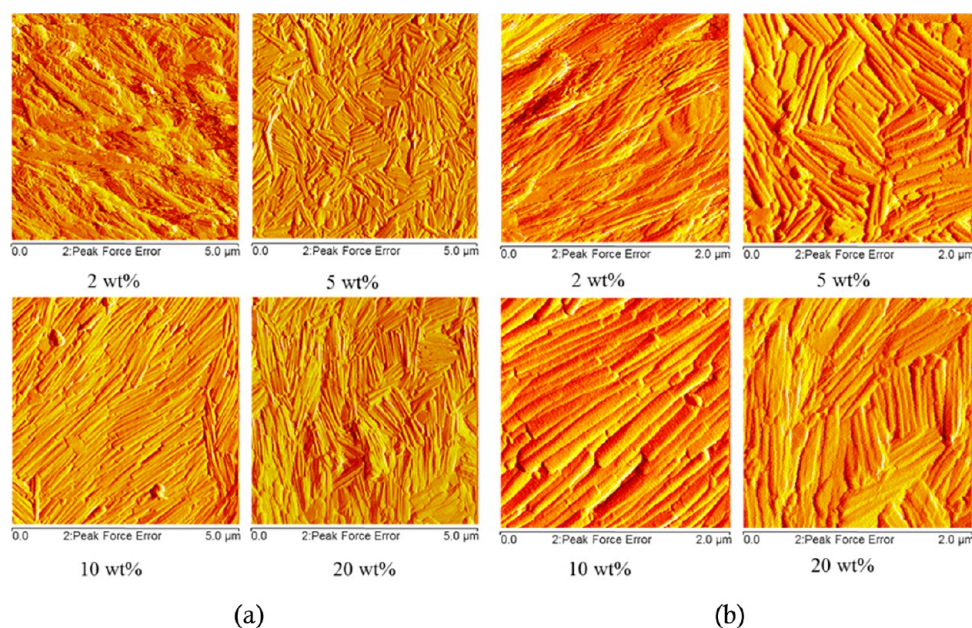
**Figure 8.** AFM image of PSS-HNTs dried at 60 °C at different scanning scopes: (a) $5 \times 5 \ \mu m^2$; (b) $2 \times 2 \ \mu m^2$.
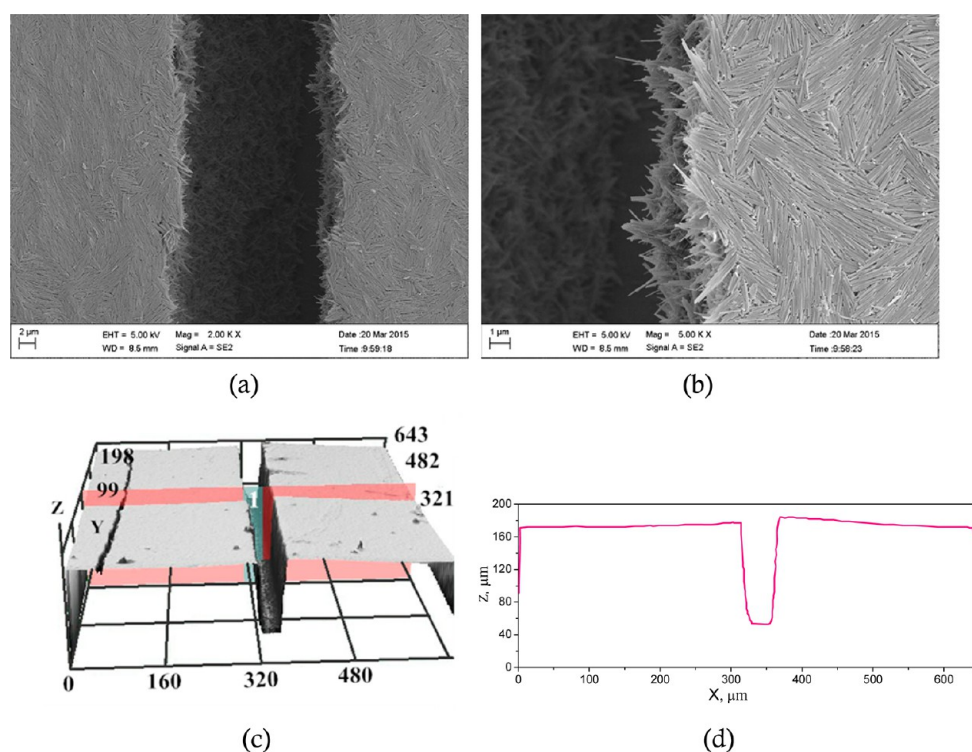


**Figure 9.** SEM (a and b), 3D morphology image (c), and the height curve of 5% PSS-HNTs dried at 60 °C showing the cracks among the stripes (d).

efficient capture of tumor cells by rough HNTs surfaces. The prepared HNTs pattern was treated by APTES to obtain a stable surface in cell culture medium. The HNTs rough surfaces can provide much higher tumor cell capture efficiency compared to blank glass surfaces, as evidenced by DAPI-staining fluorescence images (Figure 11a,b). The number of cells attached to the similar-sized areas of different surfaces was counted via ImageJ software to quantify their cell capture efficiency (Figure 11c). It can be seen that after 1, 2, and 3 h incubation, the Neuro-2a cell capture efficiency on the HNTs

rough surfaces is more than 1.7, 1.4, and 6.2 times compared to blank glass, respectively. The maximum cell capture efficiency of 88.1% is achieved for 3 h culture on the HNTs rough surface. The capture yield of the tumor cell by the prepared HNTs pattern surface can be further increased by conjugating anitibody or protein.[50−53] Previous study showed that the capture yield of MCF-7 cells on the anti-EpCAM conjugated GO film was 92 ± 4% after 45 min incubation.[50]

Interestingly, the tumor cell also exhibited differences in morphology on the rough HNTs surface and smooth glass
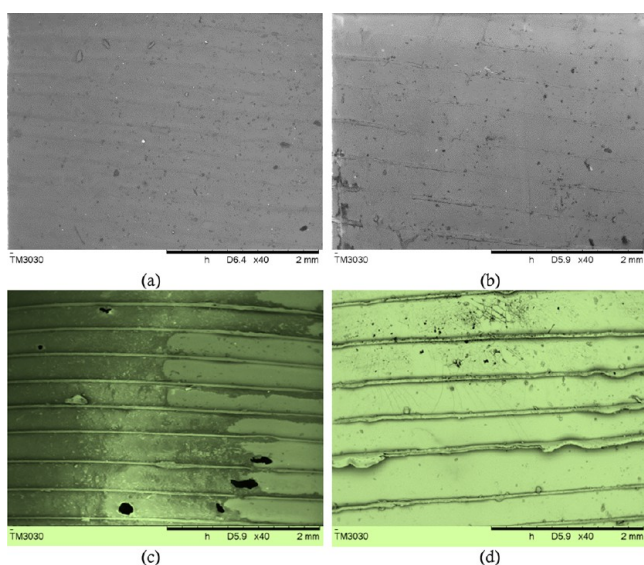
**Figure 10.** SEM image of silicone rubber molded by the pattern surfaces of 2% (a), 5% (b), 10% (c), and 20% (d) HNTs. In panels c and d, artificial coloring was used to clearly show the formed regular stripes.

surfaces as observed by SEM. From the inset of Figure 11, cells with fully extended pseudopodia attached to the HNTs surfaces can clearly be observed. However, the tumor cells on the smooth glass surface exhibit a rounded conformation without extended pseudopodia. These morphologic differences arise from the relatively high surface roughness of HNTs surfaces, and this suggests that HNTs pattern can achieve more efficient cell−substrate interactions.[48]

## 4. CONCLUSIONS

Glass capillary tubes were used to evaporate HNTs aqueous dispersion in a controlled manner for preparing a patterned surface with ordered nanotubes alignment. PSS can stabilize the HNTs dispersion by improving the surface charges of the tubes. Liquid crystal phenomenon of the dispersion is found when the HNTs aqueous dispersion concentration is higher than 10%. Rheology properties determination demonstrates that HNTs dispersions with concentrations higher than 10% show typical shear flow behavior and decreased viscosity upon shear. Upon drying the HNTs aqueous dispersion in capillary tubes, a regular pattern is formed in the wall of the tube. The width and spacing of the bands increase with HNTs dispersion concentration and decrease with drying temperature for a

given initial concentration. A model for these stripes formation is proposed, and the theoretical value highly agrees with the experimental value. SEM and AFM results show that an ordered alignment of the HNTs is found for the 10% HNTs sample. The patterned surface can be used as a model for preparing PDMS molding with regular micro-/nanostructure. The HNTs rough surfaces can provide much higher tumor cell capture efficiency compared to blank glass surfaces.

## ■ ASSOCIATED CONTENT

### Ⓢ Supporting Information

The Supporting Information is available free of charge on the ACS Publications website at DOI: 10.1021/acsami.6b01342.

> Water contact angle of PSS-HNTs coating, Tyndall effect of the PSS-HNTs dispersions, shear viscosity of PSS-HNTs dispersions, and surface roughness curve of PSS-HNTs aqueous dispersion dried at 60 °C (PDF)

## ■ AUTHOR INFORMATION

### Corresponding Authors

*(M.L.) Tel.: (86)20-85226663. Fax: (86)20-85223271. E-mail: liumx@jnu.edu.cn.
*(C.Z.) Tel.: (86)20-85226663. Fax: (86)20-85223271. E-mail: tcrz9@jnu.edu.cn.

### Notes

The authors declare no competing financial interest.

## ■ REFERENCES

(1) Byun, M.; Bowden, N. B.; Lin, Z. Hierarchically Organized Structures Engineered from Controlled Evaporative Self-Assembly. *Nano Lett.* **2010**, *10*, 3111−3117.
(2) Byun, M.; Han, W.; Qiu, F.; Bowden, N. B.; Lin, Z. Hierarchically Ordered Structures Enabled by Controlled Evaporative Self-Assembly. *Small* **2010**, *6*, 2250−2255.
(3) Han, W.; Lin, Z. Learning from "Coffee Rings": Ordered Structures Enabled by Controlled Evaporative Self-Assembly. *Angew. Chem., Int. Ed.* **2012**, *51*, 1534−1546.
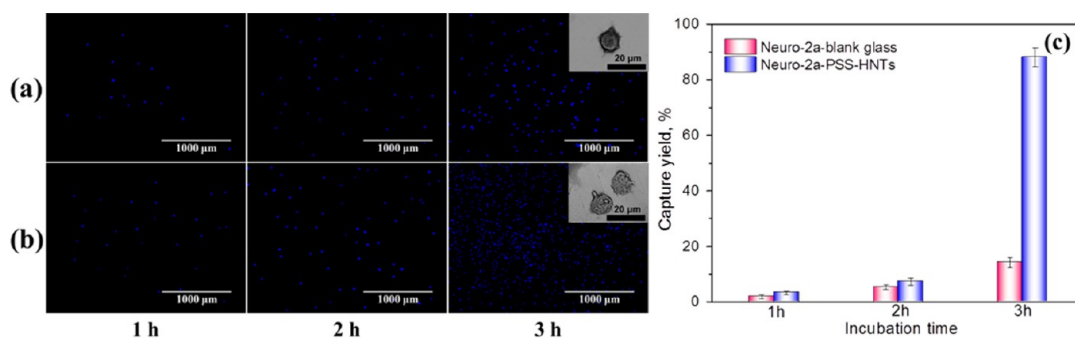


**Figure 11.** DAPI fluorescence microscopy images of captured cells on the blank glass slide (a) and PSS-HNTs surfaces (b) at different culture times; comparison of capture yield of Neuro-2a cell on glass slide and the PSS-HNTs pattern surface (c).

(4) Byun, M.; Han, W.; Li, B.; Xin, X.; Lin, Z. An Unconventional Route to Hierarchically Ordered Block Copolymers on a Gradient Patterned Surface through Controlled Evaporative Self-Assembly. *Angew. Chem., Int. Ed.* **2013**, *52*, 1122−1127.

(5) Han, W.; Byun, M.; Zhao, L.; Rzayev, J.; Lin, Z. Controlled Evaporative Self-Assembly of Hierarchically Structured Bottlebrush Block Copolymer with Nanochannels. *J. Mater. Chem.* **2011**, *21*, 14248−14253.

(6) Lin, Y.; Su, Z.; Xiao, G.; Balizan, E.; Kaur, G.; Niu, Z.; Wang, Q. Self-Assembly of Virus Particles on Flat Surfaces Via Controlled Evaporation. *Langmuir* **2011**, *27*, 1398−1402.

(7) Lin, Y.; Balizan, E.; Lee, L. A.; Niu, Z.; Wang, Q. Self-Assembly of Rodlike Bio-Nanoparticles in Capillary Tubes. *Angew. Chem., Int. Ed.* **2010**, *49*, 868−872.

(8) Lin, Y.; Su, Z.; Balizan, E.; Niu, Z.; Wang, Q. Controlled Assembly of Protein in Glass Capillary. *Langmuir* **2010**, *26*, 12803−12809.

(9) Kim, H. S.; Lee, C. H.; Sudeep, P.; Emrick, T.; Crosby, A. J. Nanoparticle Stripes, Grids, and Ribbons Produced by Flow Coating. *Adv. Mater.* **2010**, *22*, 4600−4604.

(10) Han, W.; Byun, M.; Lin, Z. Assembling and Positioning Latex Nanoparticles Via Controlled Evaporative Self-Assembly. *J. Mater. Chem.* **2011**, *21*, 16968−16972.

(11) Abkarian, M.; Nunes, J.; Stone, H. A. Colloidal Crystallization and Banding in a Cylindrical Geometry. *J. Am. Chem. Soc.* **2004**, *126*, 5978−5979.

(12) Hong, S. W.; Jeong, W.; Ko, H.; Kessler, M. R.; Tsukruk, V. V.; Lin, Z. Directed Self-Assembly of Gradient Concentric Carbon Nanotube Rings. *Adv. Funct. Mater.* **2008**, *18*, 2114−2122.

(13) Park, S.; Pitner, G.; Giri, G.; Koo, J. H.; Park, J.; Kim, K.; Wang, H.; Sinclair, R.; Wong, H. S. P.; Bao, Z. Large-Area Assembly of Densely Aligned Single-Walled Carbon Nanotubes Using Solution Shearing and Their Application to Field-Effect Transistors. *Adv. Mater.* **2015**, *27*, 2656−2662.

(14) Hong, S. W.; Xu, J.; Lin, Z. Template-Assisted Formation of Gradient Concentric Gold Rings. *Nano Lett.* **2006**, *6*, 2949−2954.

(15) Zan, X.; Feng, S.; Balizan, E.; Lin, Y.; Wang, Q. Facile Method for Large Scale Alignment of One Dimensional Nanoparticles and Control over Myoblast Orientation and Differentiation. *ACS Nano* **2013**, *7*, 8385−8396.

(16) Zhao, Y.; Cavallaro, G.; Lvov, Y. Orientation of Charged Clay Nanotubes in Evaporating Droplet Meniscus. *J. Colloid Interface Sci.* **2015**, *440*, 68−77.

(17) Hong, S. W.; Byun, M.; Lin, Z. Robust Self-Assembly of Highly Ordered Complex Structures by Controlled Evaporation of Confined Microfluids. *Angew. Chem., Int. Ed.* **2009**, *48*, 512−516.

(18) Xie, X.-L.; Mai, Y.-W.; Zhou, X.-P. Dispersion and Alignment of Carbon Nanotubes in Polymer Matrix: A Review. *Mater. Sci. Eng., R* **2005**, *49*, 89−112.

(19) Lee, C. H.; Shin, H. J.; Cho, I. H.; Kang, Y.-M.; Kim, I. A.; Park, K.-D.; Shin, J.-W. Nanofiber Alignment and Direction of Mechanical Strain Affect the Ecm Production of Human Acl Fibroblast. *Biomaterials* **2005**, *26*, 1261−1270.

(20) Li, Y.; Wu, Y. Coassembly of Graphene Oxide and Nanowires for Large-Area Nanowire Alignment. *J. Am. Chem. Soc.* **2009**, *131*, 5851−5857.

(21) Liu, M.; Jia, Z.; Jia, D.; Zhou, C. Recent Advance in Research on Halloysite Nanotubes-Polymer Nanocomposite. *Prog. Polym. Sci.* **2014**, *39*, 1498−1525.

(22) Lvov, Y.; Abdullayev, E. Functional Polymer−Clay Nanotube Composites with Sustained Release of Chemical Agents. *Prog. Polym. Sci.* **2013**, *38*, 1690−1719.

(23) Lvov, Y.; Wang, W.; Zhang, L.; Fakhrullin, R. Halloysite Clay Nanotubes for Loading and Sustained Release of Functional Compounds. *Adv. Mater.* **2016**, *28*, 1227−1250.

(24) Joussein, E.; Petit, S.; Churchman, J.; Theng, B.; Righi, D.; Delvaux, B. Halloysite Clay Minerals—a Review. *Clay Miner.* **2005**, *40*, 383−426.

(25) Vergaro, V.; Abdullayev, E.; Lvov, Y. M.; Zeitoun, A.; Cingolani, R.; Rinaldi, R.; Leporatti, S. Cytocompatibility and Uptake of Halloysite Clay Nanotubes. *Biomacromolecules* **2010**, *11*, 820−826.

(26) Ismail, H.; Pasbakhsh, P.; Fauzi, M. N. A.; Bakar, A. A. Morphological, Thermal and Tensile Properties of Halloysite Nanotubes Filled Ethylene Propylene Diene Monomer (EPDM) Nanocomposites. *Polym. Test.* **2008**, *27*, 841−850.

(27) Chiew, C. S. C.; Yeoh, H. K.; Pasbakhsh, P.; Krishnaiah, K.; Poh, P. E.; Tey, B. T.; Chan, E. S. Halloysite/Alginate Nanocomposite Beads: Kinetics, Equilibrium and Mechanism for Lead Adsorption. *Appl. Clay Sci.* **2016**, *119*, 301−310.

(28) Liu, M.; Wu, C.; Jiao, Y.; Xiong, S.; Zhou, C. Chitosan−Halloysite Nanotubes Nanocomposite Scaffolds for Tissue Engineering. *J. Mater. Chem. B* **2013**, *1*, 2078−2089.

(29) Liu, M.; Dai, L.; Shi, H.; Xiong, S.; Zhou, C. In Vitro Evaluation of Alginate/Halloysite Nanotube Composite Scaffolds for Tissue Engineering. *Mater. Sci. Eng., C* **2015**, *49*, 700−712.

(30) Tully, J.; Yendluri, R.; Lvov, Y. Halloysite Clay Nanotubes for Enzyme Immobilization. *Biomacromolecules* **2016**, *17*, 615−621.

(31) Lvov, Y. M.; Shchukin, D. G.; Mohwald, H.; Price, R. R. Halloysite Clay Nanotubes for Controlled Release of Protective Agents. *ACS Nano* **2008**, *2*, 814−820.

(32) Riela, S.; Massaro, M.; Colletti, C. G.; Bommarito, A.; Giordano, C.; Milioto, S.; Noto, R.; Poma, P.; Lazzara, G. Development and Characterization of Co-Loaded Curcumin/Triazole-Halloysite Systems and Evaluation of Their Potential Anticancer Activity. *Int. J. Pharm.* **2014**, *475*, 613−623.

(33) Massaro, M.; Colletti, C. G.; Noto, R.; Riela, S.; Poma, P.; Guernelli, S.; Parisi, F.; Milioto, S.; Lazzara, G. Pharmaceutical Properties of Supramolecular Assembly of Co-Loaded Cardanol/Triazole-Halloysite Systems. *Int. J. Pharm.* **2015**, *478*, 476−485.

(34) Massaro, M.; Riela, S.; Lo Meo, P.; Noto, R.; Cavallaro, G.; Milioto, S.; Lazzara, G. Functionalized Halloysite Multivalent Glycocluster as a New Drug Delivery System. *J. Mater. Chem. B* **2014**, *2*, 7732−7738.

(35) Fakhrullina, G. I.; Akhatova, F. S.; Lvov, Y. M.; Fakhrullin, R. F. Toxicity of Halloysite Clay Nanotubes in Vivo: A Caenorhabditis Elegans Study. *Environ. Sci.: Nano* **2015**, *2*, 54−59.

(36) Luo, Z.; Song, H.; Feng, X.; Run, M.; Cui, H.; Wu, L.; Gao, J.; Wang, Z. Liquid Crystalline Phase Behavior and Sol−Gel Transition in Aqueous Halloysite Nanotube Dispersions. *Langmuir* **2013**, *29*, 12358−12366.

(37) Zhao, X.; Xu, Z.; Xie, Y.; Zheng, B.; Kou, L.; Gao, C. Polyelectrolyte-Stabilized Graphene Oxide Liquid Crystals against Salt, Ph, and Serum. *Langmuir* **2014**, *30*, 3715−3722.

(38) Mitchell, M. J.; Castellanos, C. A.; King, M. R. Surfactant Functionalization Induces Robust, Differential Adhesion of Tumor Cells and Blood Cells to Charged Nanotube-Coated Biomaterials under Flow. *Biomaterials* **2015**, *56*, 179−186.

(39) Liu, M.; Guo, B.; Zou, Q.; Du, M.; Jia, D. Interactions between Halloysite Nanotubes and 2, 5-Bis (2-Benzoxazolyl) Thiophene and Their Effects on Reinforcement of Polypropylene/Halloysite Nanocomposites. *Nanotechnology* **2008**, *19*, 205709.

(40) Liu, P. Polymer Modified Clay Minerals: A Review. *Appl. Clay Sci.* **2007**, *38*, 64−76.

(41) Cavallaro, G.; Lazzara, G.; Milioto, S. Exploiting the Colloidal Stability and Solubilization Ability of Clay Nanotubes/Ionic Surfactant Hybrid Nanomaterials. *J. Phys. Chem. C* **2012**, *116*, 21932−21938.

(42) Gabriel, J.-C. P.; Sanchez, C.; Davidson, P. Observation of Nematic Liquid-Crystal Textures in Aqueous Gels of Smectite Clays. *J. Phys. Chem.* **1996**, *100*, 11139−11143.

(43) Hong, S. W.; Xu, J.; Xia, J.; Lin, Z.; Qiu, F.; Yang, Y. Drying Mediated Pattern Formation in a Capillary-Held Organometallic Polymer Solution. *Chem. Mater.* **2005**, *17*, 6223−6226.

(44) Dufresne, E.; Stark, D.; Greenblatt, N.; Cheng, J.; Hutchinson, J.; Mahadevan, L.; Weitz, D. Dynamics of Fracture in Drying Suspensions. *Langmuir* **2006**, *22*, 7144−7147.

(45) Han, W.; Li, B.; Lin, Z. Drying-Mediated Assembly of Colloidal Nanoparticles into Large-Scale Microchannels. *ACS Nano* **2013**, *7*, 6079−6085.

(46) Flemming, R.; Murphy, C.; Abrams, G.; Goodman, S.; Nealey, P. Effects of Synthetic Micro-and Nano-Structured Surfaces on Cell Behavior. *Biomaterials* **1999**, *20*, 573−588.

(47) Liu, X.; Wang, S. Three-Dimensional Nano-Biointerface as a New Platform for Guiding Cell Fate. *Chem. Soc. Rev.* **2014**, *43*, 2385−2401.

(48) Chen, L.; Liu, X.; Su, B.; Li, J.; Jiang, L.; Han, D.; Wang, S. Aptamer-Mediated Efficient Capture and Release of T Lymphocytes on Nanostructured Surfaces. *Adv. Mater.* **2011**, *23*, 4376−4380.

(49) Liu, X.; Chen, L.; Liu, H.; Yang, G.; Zhang, P.; Han, D.; Wang, S.; Jiang, L. Bio-Inspired Soft Polystyrene Nanotube Substrate for Rapid and Highly Efficient Breast Cancer-Cell Capture. *NPG Asia Mater.* **2013**, *5*, e63.

(50) Li, Y.; Lu, Q.; Liu, H.; Wang, J.; Zhang, P.; Liang, H.; Jiang, L.; Wang, S. Antibody-Modified Reduced Graphene Oxide Films with Extreme Sensitivity to Circulating Tumor Cells. *Adv. Mater.* **2015**, *27*, 6848−6854.

(51) Xie, M.; Lu, N.-N.; Cheng, S.-B.; Wang, X.-Y.; Wang, M.; Guo, S.; Wen, C.-Y.; Hu, J.; Pang, D.-W.; Huang, W.-H. Engineered Decomposable Multifunctional Nanobioprobes for Capture and Release of Rare Cancer Cells. *Anal. Chem.* **2014**, *86*, 4618−4626.

(52) Wang, S.; Liu, K.; Liu, J.; Yu, Z. T.-F.; Xu, X.; Zhao, L.; Lee, T.; Lee, E. K.; Reiss, J.; Lee, Y.-K.; et al. Highly Efficient Capture of Circulating Tumor Cells by Using Nanostructured Silicon Substrates with Integrated Chaotic Micromixers. *Angew. Chem., Int. Ed.* **2011**, *50*, 3084−3088.

(53) Hughes, A. D.; King, M. R. Use of Naturally Occurring Halloysite Nanotubes for Enhanced Capture of Flowing Cells. *Langmuir* **2010**, *26*, 12155−12164.